

Intelligent Reflecting Surface-Aided SWIPT: Joint Waveform, Active and Passive Beamforming Design

Yang Zhao, *Member, IEEE*, Bruno Clerckx, *Senior Member, IEEE*, and Zhenyuan Feng, *Member, IEEE*

Abstract—The performance of Simultaneous Wireless Information and Power Transfer (SWIPT) is severely restricted by the strength of the received Radio-Frequency (RF) signal. To tackle this problem, we introduce a low-power Intelligent Reflecting Surface (IRS) that compensates the propagation loss and boosts the transmission efficiency by a passive beamforming gain. This paper investigates an efficient IRS-aided SWIPT architecture where a multi-carrier multi-antenna Access Point (AP) transmits information and power simultaneously to a single-antenna user under the assist of an IRS. Considering energy harvester nonlinearity, we aim to maximize the Rate-Energy (R-E) tradeoff through a joint optimization of the transmit waveform and active beamforming at the AP, the reflection coefficients at the IRS, and the power splitting ratio at the user. Stationary solutions are achieved by the Alternating Optimization (AO) technique, where the optimal active beamforming is obtained in closed form, the passive beamforming is optimized by the Successive Convex Approximation (SCA) technique, and the waveform and splitting ratio are optimized by the Geometric Programming (GP) technique. Although practical IRS is limited to Frequency-Flat (FF) reflection, results demonstrate significant benefits of the proposed architecture based on a joint waveform and beamforming design to enlarge the R-E region of IRS-aided SWIPT.

Index Terms—Simultaneous wireless information and power transfer, intelligent reflecting surface, waveform design, active and passive beamforming.

I. INTRODUCTION

A. Simultaneous Wireless Information and Power Transfer

WITH the great advance in communication performance, a bottleneck of wireless networks has come to energy supply. Most existing mobile devices are powered by batteries that require frequent charging or replacement, which brings high maintenance cost and restricts the scale of networks. Although solar energy and inductive coupling have become popular alternatives, the former depends on the environment while the latter has a very short operation range. Simultaneous Wireless Information and Power Transfer (SWIPT) is a promising solution to connect and power mobile devices via electromagnetic (EM) waves in the Radio-Frequency (RF) band. It provides low power at μW level but broad coverage up to hundreds of meters in a sustainable and controllable manner, bringing more opportunities to the Internet of Things (IoT) and Machine to Machine (M2M) networks. The upsurge in the number of connected devices, together with the decreasing

trend in the power consumption of electronics, calls for a re-thinking of future wireless networks based on Wireless Power Transfer (WPT) and SWIPT [1].

The concept of SWIPT was first cast in [2], where the authors investigated the Rate-Energy (R-E) tradeoff for a flat Gaussian channel and typical discrete channels. Two co-localized information and power receivers were then proposed in [3], namely Time Switching (TS) that switches between Energy Harvesting (EH) and Information Decoding (ID) modes, and Power Splitting (PS) that splits the received signal into individual components. Dedicated information and energy beamforming were then investigated in [4], [5] to characterize the R-E region for multi-antenna broadcast and interference channels. On the other hand, [6] pointed out that the RF-to-Direct Current (DC) conversion efficiency depends on the input rectifier power and waveform shape. It implies that the modeling of the energy harvester, in particular its nonlinearity, has a crucial and significant impact on the waveform preference, resource allocation and system design of any wireless-powered systems [1], [6], [7]. Motivated by this, [8] derived a tractable nonlinear harvester model based on the Taylor expansion of diode I-V characteristics, then performed joint waveform and beamforming design for WPT. Simulation and experiments demonstrated that ignoring the energy harvester nonlinearity is inaccurate and emphasized the benefit of modeling such nonlinearity in real system design [9], [10]. Importantly, the joint waveform and beamforming strategy for WPT was also shown experimentally in [11] to be a key technique to expand the operation range. Beyond WPT, the work in [8] was extended to SWIPT in [12], which uniquely showed that the rectifier nonlinearity leads to radical changes to SWIPT design, namely 1) modulated and unmodulated waveforms are not equally suitable for wireless power delivery, 2) a multi-carrier unmodulated waveform superposed to a multi-carrier modulated waveform can enlarge the R-E region of SWIPT, 3) a combination of PS and TS is generally the best strategy, 4) the optimal input distribution is not the conventional Circularly Symmetric Complex Gaussian (CSCG), 5) the rectifier nonlinearity is beneficial to system performance and is essential to efficient SWIPT design. Those observations, validated experimentally in [9], led to the question: *What is the optimal input distribution for SWIPT under nonlinearity?* This question was answered in [13] for single-carrier SWIPT, and some attempts were further made in [14] for multi-carrier SWIPT. The answer sheds new light to fundamental limits of SWIPT and practical signaling (e.g. modulation and waveform) strategies. It is now well understood from [12]–[14] that, due to the nonlinearity, a combination of CSCG and on-off

The authors are with the Department of Electrical and Electronic Engineering, Imperial College London, London SW7 2AZ, U.K. (e-mail: {yang.zhao18, b.clerckx, zhenyuan.feng19}@imperial.ac.uk).

This paper has been submitted for publication.

keying in single-carrier setting and non-zero mean asymmetric inputs in multi-carrier setting lead to significantly larger R-E region compared to conventional CSCG. Recently, [15] used machine learning techniques to design SWIPT signaling under nonlinearity to complement the information-theoretic results of [13] and new modulation schemes were subsequently designed.

B. Intelligent Reflecting Surface

Intelligent Reflecting Surface (IRS) has recently emerged as a promising technique that adapts the wireless channel to increase the spectrum and energy efficiency. In practice, an IRS consists of multiple individual reflecting elements that adjust the amplitude and phase of the incident signal through passive beamforming. Different from relay and backscatter, IRS assists the primary transmission using fully passive components, thus consumes less power with no additional thermal noise but is limited to Frequency-Flat (FF) reflection. Although Frequency-Selective Surface (FSS) has received much attention for wideband communications, it is different from IRS because active FSS requires RF-chains [16] while passive FSS has fixed physical characteristics and is non-adaptive [17].

Inspired by the development of real-time reconfigurable metamaterials [18], the authors of [19] introduced a programmable metasurface that steers or polarizes the EM wave at a specific frequency to mitigate signal attenuation. Motivated by this, [20] proposed an IRS-assisted Multiple-Input Single-Output (MISO) system and jointly optimized the precoder at the Access Point (AP) and the phase shifts at the IRS to minimize the transmit power. The active and passive beamforming problem was extended to the discrete phase shift case [21] and the multi-user case [22]. Moreover, [23] investigated the coupling effect between reflection amplitude and phase shift based on the impedance equation, and [24] proposed a sequential cascaded channel estimation for Time-Division Duplex (TDD) systems. A novel dynamic passive beamforming for Orthogonal Frequency-Division Multiplexing (OFDM) systems was proposed in [25], which varies the reflection coefficients over consequent slots to enable flexible resource allocation over time-frequency Resource Blocks (RBs). In [26], a prototype IRS with 256 2-bit elements based on Positive Intrinsic-Negative (PIN) diodes was developed to support real-time high-definition video transmission at GHz and mmWave frequency.

C. IRS-Aided SWIPT

The effective channel enhancement and low power consumption of the IRS are expected to bring more opportunities to SWIPT. For a multi-user IRS-aided SWIPT system, dedicated energy beams are proved unnecessary for the Weighted Sum-Power (WSP) maximization problem [27] but essential when considering the fairness issue [28]. It was also demonstrated in [29] that Line-of-Sight (LoS) links can boost the harvested power, where the rank-deficient channels are highly correlated such that a single energy beam can satisfy all energy receivers. However, to the best of our knowledge, all existing IRS-assisted SWIPT papers focus on single-carrier transmission and consider an inaccurate and oversimplified linear energy harvester model. In this paper, we marry the benefits of joint multi-carrier

waveform and active beamforming optimization for SWIPT (accounting for nonlinearity) with the passive beamforming capability of the IRS. We ask ourselves the important question: *How to jointly exploit the spatial domain and the frequency domain efficiently through joint waveform and beamforming design to enlarge as much as possible the R-E region of IRS-aided SWIPT?* The contributions of the paper are listed as follows.

First, we introduce a novel IRS-aided SWIPT architecture based on a joint waveform, active and passive beamforming design. This architecture can be seen to IRS-aided SWIPT what [12] is to SWIPT. Specifically, we consider a IRS-aided multi-carrier downlink MISO SWIPT system where the IRS assists the information and energy transmission of a single user. A multi-carrier unmodulated power waveform (deterministic multisine) is superposed to a multi-carrier modulated information waveform to boost the energy transfer efficiency. The power and information waveforms and the active beamforming at the transmitter, the phase shifts at the IRS, and the splitting ratio at the receiver are jointly optimized to maximize the R-E tradeoff while accounting for the rectenna nonlinearity. This is the first paper to propose such a joint waveform, active and passive beamforming architecture for IRS-aided SWIPT. Note that existing IRS-aided SWIPT papers [27]–[30] focus on single-carrier transmissions and ignore the rectenna nonlinearity (and therefore assume the oversimplified and inaccurate linear model [1], [8]), which prevents from exploiting the waveform gain in SWIPT system design. On the contrary, this paper focuses on multi-carrier IRS-SWIPT and investigates the joint design of waveform, active and passive beamforming accounting for rectenna nonlinearity.

Second, we formulate an optimization for this joint waveform, active and passive beamforming design to characterize the R-E region achieved by the proposed architecture. The R-E region characterization problem is transformed into multiple energy maximization problems subject to rate constraints. Each achievable R-E pair is obtained through an Alternating Optimization (AO) algorithm that iteratively updates 1) the phase shift at the IRS, 2) the waveform, active beamforming at the transmitter and the power splitting ratio at the receiver, until convergence. On top of the SWIPT optimization by Geometric Programming (GP) [12], our IRS-aided SWIPT optimization employs a low-complexity passive beamforming algorithm based on Successive Convex Approximation (SCA) and Semidefinite Relaxation (SDR), which solves the highly non-convex problem in an efficient and reliable manner. Numerical results demonstrated SDR is tight and the proposed algorithm can always find a stationary point for all tested channel realizations under different configurations.

Third, we conduct numerical evaluations to demonstrate the advantage of the proposed IRS-aided SWIPT architecture. Despite the hardware limitations of the IRS that constraint the reflection elements to be frequency-flat, numerical results show significant R-E benefits of the proposed joint waveform and beamforming design. We confirmed the main observations of SWIPT, namely a dedicated power waveform is beneficial for multi-carrier transmission, and TS/PS are preferred at low/high SNR, carry on to the IRS-aided SWIPT. Moreover,

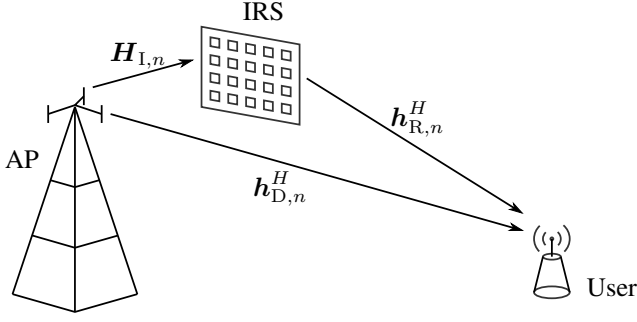


Fig. 1. An IRS-aided multi-carrier SWIPT system.

new observations are that 1) the IRS should be placed close to the transmitter or the receiver for optimal performance, 2) the number of transmit antenna and IRS elements have no noticeable impact on the optimal transceiving mode (TS/PS), 3) for active beamforming, increasing the number of transmit antennas brings a linear enhancement to the SNR and a quadratic boost to the harvested DC power, 4) for passive beamforming, increasing the number of reflecting elements provides a quadratic enhancement to the SNR and a quartic boost to the harvested DC power, 5) for narrowband transmission, the optimal active and passive beamforming are fixed for a given channel, and one only need to update the waveform and splitting ratio to draw the whole R-E boundary, 6) for broadband transmission, the frequency diversity enables rate-dependent adaptive passive beamforming to control the subchannel strength distribution and improve the R-E tradeoff.

Organization: The rest of this paper is organized as follows. Section II introduces the signal, channel, receiver, and R-E tradeoff models of the IRS-aided SWIPT system. Section III tackles the waveform, active and passive beamforming optimization. Section IV presents simulation results to evaluate the proposed design. Section V concludes the paper.

Notations: Scalars are denoted by italic letters, vectors are denoted by bold lower-case letters, and matrices are denoted by bold upper-case letters. j refers to the imaginary unit. $\mathbb{C}^{x \times y}$ denotes the subspace spanned by complex $x \times y$ matrices. $\Re\{\cdot\}$ and $\Im\{\cdot\}$ stand for the real and imaginary part of a complex number or variable, respectively. $(\cdot)^*$, $(\cdot)^T$ and $(\cdot)^H$ represent the conjugate, transpose, and conjugate transpose operators, respectively. $\mathbb{A}\{\cdot\}$ extracts the DC component of a signal, and $\mathbb{E}_X\{\cdot\}$ takes the expectation over the distribution of the random variable X (X may be omitted for simplicity). For a scalar x , $|x|$ denotes its absolute value. For a vector \mathbf{x} , $\|\mathbf{x}\|$ refers to its Euclidean norm, $\arg(\mathbf{x})$ refers to its argument vector, and $\text{diag}(\mathbf{x})$ refers to a square diagonal matrix with the elements of \mathbf{x} on the main diagonal. For a general matrix \mathbf{M} , $\text{rank}(\mathbf{M})$ denotes its rank. For a square matrix \mathbf{S} , $\text{Tr}(\mathbf{S})$ denotes its trace, and $\mathbf{S} \succeq 0$ means that \mathbf{S} is positive semi-definite. The distribution of a CSCG random vector with mean vector $\mathbf{0}$ and covariance matrix Σ is denoted by $\mathcal{CN}(\mathbf{0}, \Sigma)$, and \sim stands for "distributed as". We also denote $(\cdot)^*$ and $(\cdot)^{(i)}$ as the stationary solution and the solution at iteration i , respectively.

II. SYSTEM MODEL

As shown in Fig. 1, we propose an IRS-aided SWIPT system where a M -antenna AP delivers information and power simultaneously, through a L -element IRS, to a single-antenna user over N orthogonal evenly-spaced subbands at frequency f_n ($n = 1, \dots, N$). We consider a quasi-static block fading channel model and focus on one particular block where the channel responses are constant. It is assumed that the perfect Channel State Information (CSI) of all links with negligible training overhead is known at the AP. Two practical transceiving modes, TS and PS, are compared in terms of the achievable R-E region. Specifically, TS divides each time slot into orthogonal data and energy slots and performs a time sharing between WPT and Wireless Information Transfer (WIT). In comparison, PS splits the received signal into individual information and power streams such that the splitting ratio ρ is coupled with the waveform and beamforming design. Signals reflected by the IRS for two and more times are omitted, and the noise power is assumed too small to be harvested.

A. Transmit Signal

Denote $\tilde{x}_{I,n}(t)$ as the information symbol transmitted over subband n satisfying $\tilde{x}_{I,n} \sim \mathcal{CN}(0, 1)$. The superposed transmit signal on antenna m ($m = 1, \dots, M$) at time t is

$$x_m(t) = \Re \left\{ \sum_{n=1}^N (w_{I,n,m} \tilde{x}_{I,n}(t) + w_{P,n,m}) e^{j2\pi f_n t} \right\} \quad (1)$$

where $w_{I/P,n,m}$ denotes the weight of the information/power signal transmitted by antenna m at subband n . Stacking up the entries on all transmit antennas, we further define $\mathbf{w}_{I/P,n} \triangleq [w_{I/P,n,1}, \dots, w_{I/P,n,M}]^T \in \mathbb{C}^{M \times 1}$ and $\mathbf{x}(t) \triangleq [x_1(t), \dots, x_M(t)]^T \triangleq \mathbf{x}_I(t) + \mathbf{x}_P(t) \in \mathbb{C}^{M \times 1}$, where

$$\mathbf{x}_I(t) = \Re \left\{ \sum_{n=1}^N \mathbf{w}_{I,n} \tilde{x}_{I,n}(t) e^{j2\pi f_n t} \right\}, \quad (2)$$

$$\mathbf{x}_P(t) = \Re \left\{ \sum_{n=1}^N \mathbf{w}_{P,n} e^{j2\pi f_n t} \right\}. \quad (3)$$

B. Composite Channel

At subband n , we denote the AP-user direct channel as $\mathbf{h}_{D,n}^H \in \mathbb{C}^{1 \times M}$, AP-IRS incident channel as $\mathbf{H}_{I,n} \in \mathbb{C}^{L \times M}$, and IRS-user reflective channel as $\mathbf{h}_{R,n}^H \in \mathbb{C}^{1 \times L}$. At the IRS, element l ($l = 1, \dots, L$) redistributes the incoming signal by adjusting the reflection coefficient $\phi_l \triangleq \alpha_l e^{j\theta_l}$ with the reflection amplitude $\alpha_l \in [0, 1]$ and phase shift $\theta_l \in [0, 2\pi)$ ¹. Also, define the IRS matrix as $\Theta \triangleq \text{diag}(\phi_1, \dots, \phi_L) \in \mathbb{C}^{L \times L}$ that collects the reflection coefficients onto its main diagonal entries. The auxiliary link introduced by the IRS can be modeled as a concatenation of the AP-IRS incident channel, IRS reflection matrix, and IRS-user reflective channel. On top of this, the total composite channel is obtained by superposing

¹To investigate the performance upper bound of IRS, we suppose the reflection coefficient is maximized $\alpha_l = 1, \forall l$ while the phase shift is a continuous variable over $[0, 2\pi)$.

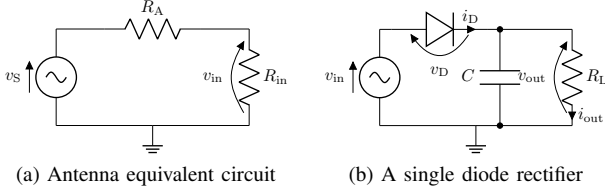


Fig. 2. Receive antenna and energy harvester circuits.

the AP-IRS-user auxiliary channel to the AP-user direct channel as

$$\mathbf{h}_n^H = \mathbf{h}_{D,n}^H + \mathbf{h}_{R,n}^H \Theta \mathbf{H}_{I,n} = \mathbf{h}_{D,n}^H + \phi^H \mathbf{V}_n \quad (4)$$

where we define $\phi \triangleq [\phi_1, \dots, \phi_L]^H \in \mathbb{C}^{L \times 1}$ and $\mathbf{V}_n \triangleq \text{diag}(\mathbf{h}_{R,n}^H) \mathbf{H}_{I,n} \in \mathbb{C}^{L \times M}$. Note the conjugate transpose in the notation of ϕ makes its entries the complex conjugate of the diagonal entries of Θ .

Remark 1. Due to hardware constraints, independent phase shift control for different frequencies is prohibited and the IRS is frequency-flat. Hence, the auxiliary channels at different frequencies cannot be simultaneously maximized and there is a tradeoff in subchannel alignment. The reflection coefficient of each IRS element is shared by the corresponding M AP-IRS-user channels over N subbands.

C. Receive Signal

At the single-antenna receiver, the total received signal $y(t) \triangleq y_I(t) + y_P(t)$ captures the contribution from information and power components over all subbands, where

$$y_I(t) = \Re \left\{ \sum_{n=1}^N \mathbf{h}_n^H \mathbf{w}_{I,n} \tilde{x}_{I,n}(t) e^{j2\pi f_n t} \right\}, \quad (5)$$

$$y_P(t) = \Re \left\{ \sum_{n=1}^N \mathbf{h}_n^H \mathbf{w}_{P,n} e^{j2\pi f_n t} \right\}. \quad (6)$$

D. Information Decoder

A major benefit of the superposed waveform is that the multisine power waveform creates no interference to the information waveform. Therefore, the achievable rate writes as

$$R(\phi, \mathbf{w}_I, \rho) = \sum_{n=1}^N \log_2 \left(1 + \frac{(1-\rho) |\mathbf{h}_n^H \mathbf{w}_{I,n}|^2}{\sigma_n^2} \right) \quad (7)$$

where ρ is the power splitting ratio for the energy harvester, σ_n^2 is the variance of the total noise (at RF-band and during RF-to-baseband conversion) on tone n . Rate (7) is achievable with either waveform cancellation or translated demodulation [12].

E. Energy Harvester

In this section, we briefly revisit a tractable nonlinear rectenna model that relates the harvester output DC current to the received waveform. Fig. 2a illustrates the equivalent circuit of an ideal antenna, where the antenna has an impedance R_A

and the incoming signal creates an voltage source $v_S(t)$. Let R_{in} be the total input impedance of the rectifier and matching network, and we assume the voltage across the matching network is negligible. When perfectly matched ($R_{in} = R_A$), the rectifier input voltage is $v_{in}(t) = y(t) \sqrt{\rho R_A}$.

Rectifiers consist of nonlinear components as diode and capacitor to produce DC output and store energy [31]. Consider a simplified rectifier model in Fig. 2b where a single series diode is followed by a low-pass filter with a parallel load. As detailed in [8], [12], a truncated Taylor expansion of the diode I-V characteristic equation suggests that, when the subband frequencies are evenly-spaced, maximizing the average output DC current is equivalent to maximizing a monotonic function ²

$$z(\phi, \mathbf{w}_I, \mathbf{w}_P, \rho) = \sum_{i \text{ even}, i \geq 2}^{n_0} k_i \rho^{i/2} R_A^{i/2} \mathbb{E} \{ \mathbb{A} \{ y(t)^i \} \} \quad (8)$$

where n_0 is the truncation order and $k_i \triangleq i_S / i! (n' v_T)^i$ is the diode coefficient (i_S is the reverse bias saturation current, n' is the diode ideality factor, v_T is the thermal voltage). With a slight abuse of notation, we refer to z as the average output DC current in the following context. It can be observed that the traditional linear harvester model, where the output DC power equals the sum of the power harvested on each frequency, is a special case of (8) with $n_0 = 2$. However, due to the coupling effect among different frequencies, some high-order AC components compensate each other and further contribute to the output DC power. In other words, even-order terms with $i \geq 4$ account for the diode nonlinear behavior. For simplicity, we choose $n_0 = 4$ to investigate the fundamental rectifier nonlinearity, and define $\beta_2 \triangleq k_2 R_A$, $\beta_4 \triangleq k_4 R_A^2$ to rewrite z by (9). Note that $\mathbb{E} \{ |\tilde{x}_{I,n}|^2 \} = 1$ but $\mathbb{E} \{ |\tilde{x}_{I,n}|^4 \} = 2$, which can be interpreted as a modulation gain on the nonlinear terms of the output DC current. Inspired by [32], we stack up the channel and waveform vectors over all subbands as $\mathbf{h} \triangleq [\mathbf{h}_1^T, \dots, \mathbf{h}_N^T]^T \in \mathbb{C}^{MN \times 1}$ and $\mathbf{w}_{I/P} \triangleq [\mathbf{w}_{I/P,1}^T, \dots, \mathbf{w}_{I/P,N}^T]^T \in \mathbb{C}^{MN \times 1}$, then define $\mathbf{W}_{I/P} \triangleq \mathbf{w}_{I/P} \mathbf{w}_{I/P}^H \in \mathbb{C}^{MN \times MN}$. As illustrated by Fig. 3, $\mathbf{W}_{I/P}$ can be divided into $N \times N$ blocks of size $M \times M$, and we let $\mathbf{W}_{I/P,k}$ keep its k -th ($k = -N + 1, \dots, N - 1$) block diagonal and set all other blocks to $\mathbf{0}^{M \times M}$. Hence, the components of the average output DC current z can be expressed in (10) – (13).

F. Rate-Energy Region

The achievable R-E region is defined as

$$C_{R_{ID}-I_{EH}}(P) \triangleq \left\{ (R_{ID}, I_{EH}) : R_{ID} \leq R, I_{EH} \leq z, \frac{1}{2} (\|\mathbf{w}_I\|^2 + \|\mathbf{w}_P\|^2) \leq P \right\} \quad (14)$$

where P is the average transmit power budget and the coefficient $1/2$ converts the peak power of sine waves to the average power.

²Note that this small-signal expansion model is only valid for the non-linear operation region of the diode, and the I-V relationship would be linear if the diode behavior is dominated by the load [8].



Fig. 3. $\mathbf{W}_{I/P}$ consists of $N \times N$ blocks of size $M \times M$. $\mathbf{W}_{I/P,k}$ keeps the k -th block diagonal of $\mathbf{W}_{I/P}$ and nulls all remaining blocks. Solid, dashed and dotted blocks correspond to $k > 0$, $k = 0$ and $k < 0$, respectively. For $\mathbf{w}_{I/P,n_1} \mathbf{w}_{I/P,n_2}^H$, the k -th block diagonal satisfies $k = n_2 - n_1$.

III. PROBLEM FORMULATION

We characterize the R-E region through a current maximization problem subject to transmit power, IRS magnitude, and rate constraints

$$\max_{\phi, \mathbf{w}_I, \mathbf{w}_P, \rho} z(\phi, \mathbf{w}_I, \mathbf{w}_P, \rho) \quad (15a)$$

$$\text{s.t.} \quad \frac{1}{2} (\|\mathbf{w}_I\|^2 + \|\mathbf{w}_P\|^2) \leq P, \quad (15b)$$

$$R(\phi, \mathbf{w}_I, \rho) \geq \bar{R}, \quad (15c)$$

$$|\phi_l| = 1, \quad l = 1, \dots, L, \quad (15d)$$

$$0 \leq \rho \leq 1. \quad (15e)$$

Problem (15) is intricate with coupled variables in non-convex expressions (15a), (15c), (15d). To obtain a feasible solution, we propose an AO algorithm that iteratively updates 1) the phase shift at the IRS, 2) the waveform, active beamforming at the transmitter and the power splitting ratio at the receiver, until convergence.

Remark 2. As information and power transfer prefer different subchannel strength distribution, the frequency-flat characteristic of the IRS introduces a resource allocation problem. Following Remark 1, if the IRS is frequency-selective and there is only one transmit antenna, then each reflecting element can

simultaneously align the corresponding AP-IRS-user channel with the AP-user channel at all subbands. In this case, the strengths of all subchannels are maximized so that the joint design would follow straightforwardly from existing SWIPT work [12].

A. IRS Phase Shift

In this section, the IRS phase shift ϕ is optimized for any given waveform $\mathbf{w}_{I/P}$ and splitting ratio ρ . We observe that

$$\begin{aligned} |\mathbf{h}_n^H \mathbf{w}_{I,n}|^2 &= \mathbf{w}_{I,n}^H \mathbf{h}_n \mathbf{h}_n^H \mathbf{w}_{I,n} \\ &= \mathbf{w}_{I,n}^H (\mathbf{h}_{D,n} + \mathbf{V}_n^H \phi) (\mathbf{h}_{D,n} + \phi^H \mathbf{V}_n) \mathbf{w}_{I,n} \\ &= \mathbf{w}_{I,n}^H \mathbf{M}_n^H \Phi \mathbf{M}_n \mathbf{w}_{I,n} \\ &= \text{Tr}(\mathbf{M}_n \mathbf{w}_{I,n} \mathbf{w}_{I,n}^H \mathbf{M}_n^H \Phi) \\ &= \text{Tr}(\mathbf{C}_n \Phi) \end{aligned} \quad (16)$$

where $\mathbf{M}_n \triangleq [\mathbf{V}_n^H, \mathbf{h}_{D,n}]^H \in \mathbb{C}^{(L+1) \times M}$, t is an auxiliary variable with unit modulus, $\bar{\phi} \triangleq [\phi^H, t]^H \in \mathbb{C}^{(L+1) \times 1}$, $\Phi \triangleq \bar{\phi} \bar{\phi}^H \in \mathbb{C}^{(L+1) \times (L+1)}$, $\mathbf{C}_n \triangleq \mathbf{M}_n \mathbf{w}_{I,n} \mathbf{w}_{I,n}^H \mathbf{M}_n^H \in$

$$z(\phi, \mathbf{w}_I, \mathbf{w}_P, \rho) = \beta_2 \rho \left(\mathbb{E} \{ \mathbb{A} \{ y_I^2(t) \} \} + \mathbb{A} \{ y_P^2(t) \} \right) + \beta_4 \rho^2 \left(\mathbb{E} \{ \mathbb{A} \{ y_I^4(t) \} \} + \mathbb{A} \{ y_P^4(t) \} + 6 \mathbb{E} \{ \mathbb{A} \{ y_I^2(t) \} \} \mathbb{A} \{ y_P^2(t) \} \right). \quad (9)$$

$$\mathbb{E} \{ \mathbb{A} \{ y_I^2(t) \} \} = \frac{1}{2} \sum_{n=1}^N (\mathbf{h}_n^H \mathbf{w}_{I,n}) (\mathbf{h}_n^H \mathbf{w}_{I,n})^* = \frac{1}{2} \mathbf{h}^H \mathbf{W}_{I,0} \mathbf{h}, \quad (10)$$

$$\mathbb{E} \{ \mathbb{A} \{ y_I^4(t) \} \} = \frac{3}{4} \left(\sum_{n=1}^N (\mathbf{h}_n^H \mathbf{w}_{I,n}) (\mathbf{h}_n^H \mathbf{w}_{I,n})^* \right)^2 = \frac{3}{4} (\mathbf{h}^H \mathbf{W}_{I,0} \mathbf{h})^2, \quad (11)$$

$$\mathbb{A} \{ y_P^2(t) \} = \frac{1}{2} \sum_{n=1}^N (\mathbf{h}_n^H \mathbf{w}_{P,n}) (\mathbf{h}_n^H \mathbf{w}_{P,n})^* = \frac{1}{2} \mathbf{h}^H \mathbf{W}_{P,0} \mathbf{h}, \quad (12)$$

$$\mathbb{A} \{ y_P^4(t) \} = \frac{3}{8} \sum_{\substack{n_1, n_2, n_3, n_4 \\ n_1 + n_2 = n_3 + n_4}} (\mathbf{h}_{n_1}^H \mathbf{w}_{P,n_1}) (\mathbf{h}_{n_2}^H \mathbf{w}_{P,n_2}) (\mathbf{h}_{n_3}^H \mathbf{w}_{P,n_3})^* (\mathbf{h}_{n_4}^H \mathbf{w}_{P,n_4})^* = \frac{3}{8} \sum_{k=-N+1}^{N-1} (\mathbf{h}^H \mathbf{W}_{P,k} \mathbf{h}) (\mathbf{h}^H \mathbf{W}_{P,k} \mathbf{h})^*. \quad (13)$$

$\mathbb{C}^{(L+1) \times (L+1)}$. On the other hand, we define $t_{I/P,k}$ as

$$\begin{aligned} t_{I/P,k} &\triangleq \mathbf{h}^H \mathbf{W}_{I/P,k} \mathbf{h} \\ &= \text{Tr}(\mathbf{h} \mathbf{h}^H \mathbf{W}_{I/P,k}) \\ &= \text{Tr}((\mathbf{h}_D + \mathbf{V}^H \boldsymbol{\phi})(\mathbf{h}_D^H + \boldsymbol{\phi}^H \mathbf{V}) \mathbf{W}_{I/P,k}) \\ &= \text{Tr}(\mathbf{M}^H \boldsymbol{\Phi} \mathbf{M} \mathbf{W}_{I/P,k}) \\ &= \text{Tr}(\mathbf{M} \mathbf{W}_{I/P,k} \mathbf{M}^H \boldsymbol{\Phi}) \\ &= \text{Tr}(\mathbf{C}_{I/P,k} \boldsymbol{\Phi}) \end{aligned} \quad (17)$$

where $\mathbf{V} \triangleq [\mathbf{V}_1, \dots, \mathbf{V}_N] \in \mathbb{C}^{L \times MN}$, $\mathbf{M} \triangleq [\mathbf{V}^H, \mathbf{h}_D]^H \in \mathbb{C}^{(L+1) \times MN}$, $\mathbf{C}_{I/P,k} \triangleq \mathbf{M} \mathbf{W}_{I/P,k} \mathbf{M}^H \in \mathbb{C}^{(L+1) \times (L+1)}$. Therefore, we can rewrite the rate and average DC current expressions as

$$\begin{aligned} R(\boldsymbol{\Phi}) &= \sum_{n=1}^N \log_2 \left(1 + \frac{(1-\rho) \text{Tr}(\mathbf{C}_n \boldsymbol{\Phi})}{\sigma_n^2} \right), \quad (18) \\ z(\boldsymbol{\Phi}) &= \frac{1}{2} \beta_2 \rho (t_{I,0} + t_{P,0}) \\ &\quad + \frac{3}{8} \beta_4 \rho^2 \left(2t_{I,0}^2 + \sum_{k=-N+1}^{N-1} t_{P,k} t_{P,k}^* \right) \\ &\quad + \frac{3}{2} \beta_4 \rho^2 t_{I,0} t_{P,0}. \end{aligned} \quad (19)$$

To maximize non-concave expression (19), we propose a SCA algorithm that approximate the second-order terms by their first-order Taylor expansion [33]. Based on the solution at iteration $i-1$, the approximations at iteration i are

$$(t_{I,0}^{(i)})^2 \geq 2t_{I,0}^{(i)} t_{I,0}^{(i-1)} - (t_{I,0}^{(i-1)})^2, \quad (20)$$

$$t_{P,k}^{(i)} (t_{P,k}^{(i)})^* \geq 2\Re \left\{ t_{P,k}^{(i)} (t_{P,k}^{(i-1)})^* \right\} - t_{P,k}^{(i-1)} (t_{P,k}^{(i-1)})^*, \quad (21)$$

$$\begin{aligned} t_{I,0}^{(i)} t_{P,0}^{(i)} &= \frac{1}{4} (t_{I,0}^{(i)} + t_{P,0}^{(i)})^2 - \frac{1}{4} (t_{I,0}^{(i)} - t_{P,0}^{(i)})^2 \\ &\geq \frac{1}{2} (t_{I,0}^{(i)} + t_{P,0}^{(i)}) (t_{I,0}^{(i-1)} + t_{P,0}^{(i-1)}) \\ &\quad - \frac{1}{4} (t_{I,0}^{(i-1)} + t_{P,0}^{(i-1)})^2 - \frac{1}{4} (t_{I,0}^{(i)} - t_{P,0}^{(i)})^2 \end{aligned} \quad (22)$$

which provide lower bounds to the corresponding terms in (19). Hence, the objective function is approximated by $\tilde{z}(\boldsymbol{\Phi}^{(i)})$ in (23), and problem (15) is transformed to

$$\max_{\boldsymbol{\Phi}} \quad \tilde{z}(\boldsymbol{\Phi}) \quad (24a)$$

$$\text{s.t.} \quad R(\boldsymbol{\Phi}) \geq \bar{R}, \quad (24b)$$

$$\boldsymbol{\Phi}_{l',l'} = 1, \quad l' = 1, \dots, L+1, \quad (24c)$$

$$\boldsymbol{\Phi} \succeq 0, \quad (24d)$$

$$\text{rank}(\boldsymbol{\Phi}) = 1. \quad (24e)$$

Algorithm 1 SCA: IRS Phase Shift.

```

1: Input  $\beta_2, \beta_4, \mathbf{h}_{D,n}, \mathbf{H}_{I,n}, \mathbf{h}_{R,n}, \mathbf{w}_{I/P}, \rho, \sigma_n, \bar{R}, Q, \epsilon, \forall n$ 
2: Construct  $\mathbf{M}, \mathbf{M}_n, \mathbf{C}_n, \mathbf{C}_{I/P,k}, \forall n, k$ 
3: Initialize  $i \leftarrow 0, \boldsymbol{\Phi}^{(0)}, t_{I/P,k}^{(0)}, \forall k$ 
4: Repeat
5:    $i \leftarrow i + 1$ 
6:   Obtain  $\boldsymbol{\Phi}^{(i)}, t_{I/P,k}^{(i)}, \forall k$  by solving problem (24)
7:   Compute  $z^{(i)}$  by (19)
8: Until  $|z^{(i)} - z^{(i-1)}| \leq \epsilon$ 
9: Set  $\boldsymbol{\Phi}^* = \boldsymbol{\Phi}^{(i)}$ 
10: If  $\text{rank}(\boldsymbol{\Phi}^*) = 1$  Then
11:   Obtain  $\boldsymbol{\phi}^*$  by EVD,  $\boldsymbol{\Phi}^* = \boldsymbol{\phi}^* (\boldsymbol{\phi}^*)^H$ 
12: Else
13:   Obtain  $\mathbf{U}, \boldsymbol{\Sigma}$  by EVD,  $\boldsymbol{\Phi}^* = \mathbf{U} \boldsymbol{\Sigma} \mathbf{U}^H$ 
14:   Generate  $\mathbf{r}_q \sim \mathcal{CN}(\mathbf{0}, \mathbf{I}_{L+1}), \forall q$ 
15:   Construct  $\bar{\boldsymbol{\phi}}_q = e^{j \arg(\mathbf{U} \boldsymbol{\Sigma}^{1/2} \mathbf{r}_q)}, \boldsymbol{\Phi}_q = \bar{\boldsymbol{\phi}}_q \bar{\boldsymbol{\phi}}_q^H, \forall q$ 
16:   Set  $q^* = \arg \max_q z(\boldsymbol{\Phi}_q), \bar{\boldsymbol{\phi}}^* = \bar{\boldsymbol{\phi}}_{q^*}$ 
17: End If
18: Set  $\theta_l^* = \arg(\bar{\boldsymbol{\phi}}_l^* / \bar{\boldsymbol{\phi}}_{L+1}^*), \forall l, \boldsymbol{\phi}^* = [e^{j\theta_1^*}, \dots, e^{j\theta_L^*}]^H$ 
19: Output  $\boldsymbol{\phi}^*$ 

```

Problem (24) is not a standard Semidefinite Programming (SDP). If we relax the rank constraint (24e) to formulate a convex problem, there is no guarantee that $\boldsymbol{\Phi}^*$ is rank-1 and the extracted rank-1 solution $\boldsymbol{\phi}^*$ be a stationary point of the original problem (15). In Section IV, we numerically show that $\boldsymbol{\Phi}^*$ is rank-1 for all tested channel realizations under different configurations, where the performance loss by SDR is negligible. If $\boldsymbol{\Phi}^*$ is rank-1, the augmented phase shift vector $\bar{\boldsymbol{\phi}}^*$ can be obtained by Eigenvalue Decomposition (EVD). Otherwise, a suboptimal solution can be extracted via Gaussian randomization method [34], where we perform EVD $\boldsymbol{\Phi}^* = \mathbf{U} \boldsymbol{\Sigma} \mathbf{U}^H$, generate Q CSCG random vectors $\mathbf{r}_q \sim \mathcal{CN}(\mathbf{0}, \mathbf{I}_{L+1}), q = 1, \dots, Q$, construct the corresponding candidates $\bar{\boldsymbol{\phi}}_q = e^{j \arg(\mathbf{U} \boldsymbol{\Sigma}^{1/2} \mathbf{r}_q)}$, and choose the one that maximizes the objective function (24a). Finally, the phase shifts are retrieved by $\theta_l^* = \arg(\bar{\boldsymbol{\phi}}_l^* / \bar{\boldsymbol{\phi}}_{L+1}^*), l = 1, \dots, L$. Problem (24) without constraint (24e) can be solved by existing optimization tools such as CVX [35]. The SCA algorithm for the passive beamforming optimization is summarized in Algorithm 1.

B. Waveform, Active Beamforming and Splitting Ratio

Next, we jointly optimize the waveform and active beamforming $\mathbf{w}_{I/P}$ together with the splitting ratio ρ for any given IRS phase shift $\boldsymbol{\phi}$. As pointed out in [12], the waveform design

$$\begin{aligned} \tilde{z}(\boldsymbol{\Phi}^{(i)}) &= \frac{1}{2} \beta_2 \rho (t_{I,0}^{(i)} + t_{P,0}^{(i)}) \\ &\quad + \frac{3}{8} \beta_4 \rho^2 \left(4t_{I,0}^{(i)} t_{I,0}^{(i-1)} - 2(t_{I,0}^{(i-1)})^2 + \sum_{k=-N+1}^{N-1} 2\Re \left\{ t_{P,k}^{(i)} (t_{P,k}^{(i-1)})^* \right\} - t_{P,k}^{(i-1)} (t_{P,k}^{(i-1)})^* \right) \\ &\quad + \frac{3}{2} \beta_4 \rho^2 \left(\frac{1}{2} (t_{I,0}^{(i)} + t_{P,0}^{(i)}) (t_{I,0}^{(i-1)} + t_{P,0}^{(i-1)}) - \frac{1}{4} (t_{I,0}^{(i-1)} + t_{P,0}^{(i-1)})^2 - \frac{1}{4} (t_{I,0}^{(i)} - t_{P,0}^{(i)})^2 \right). \end{aligned} \quad (23)$$

in the frequency domain and the active beamformer in the spatial domain can be decoupled without performance loss, and the optimal spatial weight is given by Maximum-Ratio Transmission (MRT) beamformer

$$\mathbf{w}_{I/P,n} = s_{I/P,n} \frac{\mathbf{h}_n}{\|\mathbf{h}_n\|}. \quad (25)$$

That is to say, for single-user MISO SWIPT, the optimal active beamformer is MRT and we only need to determine the amplitudes $s_{I/P,n}$ at different tones. Hence, the original waveform and active beamforming optimization with $2MN$ complex variables is converted into a power allocation problem with $2N$ nonnegative real variables. Define $\mathbf{s}_{I/P} \triangleq [s_{I/P,1}, \dots, s_{I/P,N}]^T \in \mathbb{C}^{N \times 1}$. At subband n , the effective channel strength is given by $\|\mathbf{h}_n\|$, and the power allocated to the modulated and unmodulated waveform are given by $s_{I,n}^2$ and $s_{P,n}^2$, respectively. With such an active beamformer selection, we have $\mathbf{h}_n^H \mathbf{w}_{I,n} = |\mathbf{h}_n^H \mathbf{w}_{I,n}| = \|\mathbf{h}_n\| s_{I,n}$ such that the rate and objective functions further reduce to (26) and (27), respectively.

$$R(\mathbf{s}_I, \rho) = \log_2 \left(\prod_{n=1}^N \left(1 + \frac{(1-\rho)\|\mathbf{h}_n\|^2 s_{I,n}^2}{\sigma_n^2} \right) \right). \quad (26)$$

Therefore, problem (15) is reduced to an amplitude optimization issue

$$\max_{\mathbf{s}_I, \mathbf{s}_P, \rho} z(\mathbf{s}_I, \mathbf{s}_P, \rho) \quad (28a)$$

$$\text{s.t.} \quad \frac{1}{2} (\|\mathbf{s}_I\|^2 + \|\mathbf{s}_P\|^2) \leq P, \quad (28b)$$

$$R(\mathbf{s}_I, \rho) \geq \bar{R}. \quad (28c)$$

Since problem (28) involves the production of nonnegative real variables, we introduce auxiliary variables $t', \bar{\rho}$ and transform it into a reversed GP

$$\min_{\mathbf{s}_I, \mathbf{s}_P, \rho, \bar{\rho}, t'} \frac{1}{t'} \quad (29a)$$

$$\text{s.t.} \quad \frac{1}{2} (\|\mathbf{s}_I\|^2 + \|\mathbf{s}_P\|^2) \leq P, \quad (29b)$$

$$\frac{t'}{z(\mathbf{s}_I, \mathbf{s}_P, \rho)} \leq 1, \quad (29c)$$

$$\frac{2\bar{R}}{\prod_{n=1}^N \left(1 + \bar{\rho} \|\mathbf{h}_n\|^2 s_{I,n}^2 / \sigma_n^2 \right)} \leq 1, \quad (29d)$$

$$\rho + \bar{\rho} \leq 1. \quad (29e)$$

The denominators of (29c), (29d) are posynomials [36] that can be further decomposed as

$$z(\mathbf{s}_I, \mathbf{s}_P, \rho) \triangleq \sum_{m_P} g_{m_P}(\mathbf{s}_I, \mathbf{s}_P, \rho), \quad (30)$$

$$1 + \frac{\bar{\rho} \|\mathbf{h}_n\|^2 s_{I,n}^2}{\sigma_n^2} \triangleq \sum_{m_{I,n}} g_{m_{I,n}}(s_{I,n}, \bar{\rho}) \quad (31)$$

where $m_P = (2N^3 + 6N^2 + 7N)/3$, $m_{I,n} = 2$ are the number of monomials. Following [37], we upper bound posynomials (30) and (31) by Arithmetic Mean-Geometric Mean (AM-GM) inequality such that problem (29) reduces to

$$\min_{\mathbf{s}_I, \mathbf{s}_P, \rho, \bar{\rho}, t'} \frac{1}{t'} \quad (32a)$$

$$\text{s.t.} \quad \frac{1}{2} (\|\mathbf{s}_I\|^2 + \|\mathbf{s}_P\|^2) \leq P, \quad (32b)$$

$$t' \prod_{m_P} \left(\frac{g_{m_P}(\mathbf{s}_I, \mathbf{s}_P, \rho)}{\gamma_{m_P}} \right)^{-\gamma_{m_P}} \leq 1, \quad (32c)$$

$$2\bar{R} \prod_n \prod_{m_{I,n}} \left(\frac{g_{m_{I,n}}(s_{I,n}, \bar{\rho})}{\gamma_{m_{I,n}}} \right)^{-\gamma_{m_{I,n}}} \leq 1, \quad (32d)$$

$$\rho + \bar{\rho} \leq 1 \quad (32e)$$

where $\gamma_{m_P}, \gamma_{m_{I,n}} \geq 0$, $\sum_{m_P} \gamma_{m_P} = \sum_{m_{I,n}} \gamma_{m_{I,n}} = 1$. The tightness of the AM-GM inequality depends on $\{\gamma_{m_P}, \gamma_{m_{I,n}}\}$ that require successive update. As suggested in [12], a feasible choice at iteration i is

$$\gamma_{m_P}^{(i)} = \frac{g_{m_P}(\mathbf{s}_I^{(i-1)}, \mathbf{s}_P^{(i-1)}, \rho^{(i-1)})}{z(\mathbf{s}_I^{(i-1)}, \mathbf{s}_P^{(i-1)}, \rho^{(i-1)})}, \quad (33)$$

$$\gamma_{m_{I,n}}^{(i)} = \frac{g_{m_{I,n}}(s_{I,n}^{(i-1)}, \bar{\rho}^{(i-1)})}{1 + \bar{\rho}^{(i-1)} \|\mathbf{h}_n\|^2 (s_{I,n}^{(i-1)})^2 / \sigma_n^2}. \quad (34)$$

$\mathbf{s}_I, \mathbf{s}_P, \rho$ are updated iteratively until convergence. Problem (32) can be solved by existing optimization tools such as CVX [35]. The GP algorithm of the waveform, active beamforming and splitting ratio optimization is summarized in Algorithm 2.

C. Alternating Optimization

For any direct, incident and reflective channels, we iteratively update the passive beamforming ϕ by Algorithm 1, and the waveform, active beamforming $\mathbf{w}_{I/P}$ together with the splitting ratio ρ by Algorithm 2 until convergence. The AO algorithm is summarized in Algorithm 3.

$$\begin{aligned} z(\mathbf{s}_I, \mathbf{s}_P, \rho) = & \frac{1}{2} \beta_2 \rho \sum_{n=1}^N \|\mathbf{h}_n\|^2 (s_{I,n}^2 + s_{P,n}^2) \\ & + \frac{3}{8} \beta_4 \rho^2 \left(2 \sum_{n_1, n_2} \prod_{j=1}^2 \|\mathbf{h}_{n_j}\|^2 s_{I,n_j}^2 + \sum_{\substack{n_1, n_2, n_3, n_4 \\ n_1 + n_2 = n_3 + n_4}} \prod_{j=1}^4 \|\mathbf{h}_{n_j}\| s_{P,n_j} \right) \\ & + \frac{3}{2} \beta_4 \rho^2 \left(\sum_{n_1, n_2} \|\mathbf{h}_{n_1}\|^2 \|\mathbf{h}_{n_2}\|^2 s_{I,n_1}^2 s_{P,n_2}^2 \right). \end{aligned} \quad (27)$$

Algorithm 2 GP: Waveform, Active Beamforming and Splitting Ratio.

```

1: Input  $\beta_2, \beta_4, \mathbf{h}, P, \sigma_n, \bar{R}, \epsilon, \forall n$ 
2: Initialize  $i \leftarrow 0, \mathbf{s}_{I/P}^{(0)}, \rho^{(0)}$ 
3: Repeat
4:    $i \leftarrow i + 1$ 
5:   Update  $\{\gamma_{m_P}^{(i)}, \gamma_{m_{I,n}}^{(i)}\}, \forall n$  by (33), (34)
6:   Obtain  $\mathbf{s}_{I/P}^{(i)}, \rho^{(i)}$  by solving problem (32)
7:   Compute  $z^{(i)}$  by (27)
8: Until  $|z^{(i)} - z^{(i-1)}| \leq \epsilon$ 
9: Set  $\mathbf{s}_{I/P}^* = \mathbf{s}_{I/P}^{(i)}, \rho^* = \rho^{(i)}$ , retrieve  $\mathbf{w}_{I/P}^*$  by (25)
10: Output  $\mathbf{w}_I^*, \mathbf{w}_P^*, \rho^*$ 

```

Algorithm 3 AO: Waveform, Active and Passive Beamforming, and Splitting Ratio.

```

1: Input  $\beta_2, \beta_4, \mathbf{h}_{D,n}, \mathbf{H}_{I,n}, \mathbf{h}_{R,n}, P, \sigma_n, \bar{R}, Q, \epsilon, \forall n$ 
2: Initialize  $i \leftarrow 0, \phi^{(0)}, \mathbf{w}_{I/P}^{(0)}, \rho^{(0)}$ 
3: Repeat
4:    $i \leftarrow i + 1$ 
5:   Fix  $\mathbf{w}_{I/P}^{(i-1)}, \rho^{(i-1)}$  and obtain  $\phi^{(i)}$  by Algorithm 1
6:   Fix  $\phi^{(i)}$ , update  $\mathbf{h}_n^{(i)}, \forall n$  by (4), obtain  $\mathbf{w}_{I/P}^{(i)}, \rho^{(i)}$  by
     Algorithm 2
7:   Compute  $z^{(i)}$  by (19)
8: Until  $|z^{(i)} - z^{(i-1)}| \leq \epsilon$ 
9: Output  $\phi^*, \mathbf{w}_I^*, \mathbf{w}_P^*, \rho^*$ 

```

D. Convergence

Proposition 1. For any feasible initial point, the proposed SCA-based Algorithm 1 can provide a feasible Φ^* that satisfies the KKT conditions, although there is no guarantee Φ^* is rank-1.

Proof. The objective function (24a) is non-decreasing over iterations because the solution of problem (24) at iteration $i - 1$ is still a feasible point at iteration i . Moreover, the sequence $\{\tilde{z}(\Phi^{(i)})\}_{i=1}^\infty$ is bounded above due to the unit-modulus constraint (24c). Thus, Algorithm 1 is guaranteed to converge. To prove $\Phi^{(i)}$ converges to the set of stationary points of IRS subproblem, we notice that the SCA-based Algorithm 1 is indeed an inner approximation algorithm [38], since $\tilde{z}(\Phi) \leq z(\Phi)$, $\partial \tilde{z}(\Phi^{(i)})/\partial \Phi = \partial z(\Phi^{(i)})/\partial \Phi$ and the approximation (20) – (22) are asymptotically tight as $i \rightarrow \infty$ [39]. Therefore, Algorithm 1 is guaranteed to provide a feasible Φ^* that satisfies the KKT conditions. \square

Proposition 2. For any feasible initial point, the GP-based Algorithm 2 is guaranteed to converge to a stationary point of the waveform, active beamforming and splitting ratio subproblem.

Proof. See [8], [12]. \square

Proposition 3. Suppose Φ is rank-1, every limit point $(\phi^*, \mathbf{w}_I^*, \mathbf{w}_P^*, \rho^*)$ of the proposed alternating algorithm is a stationary point of the original problem (15).

Proof. The objective function (15a) is non-decreasing over iterations of Algorithm 3, which is also upper-bounded due to the unit-modulus constraint (15d) and the average transmit

power constraint (15b). If Φ is rank-1, then ϕ can be obtained by EVD without performance loss, and the sequence $\{\phi^{(i)}, \mathbf{w}_I^{(i)}, \mathbf{w}_P^{(i)}, \rho^{(i)}\}$ generated by alternatively optimizing ϕ and $\mathbf{w}_I, \mathbf{w}_P, \rho$ has limit points and Algorithm 3 is guaranteed to converge. As demonstrated in [40], the solution is a stationary point of problem (15). \square

E. Low-Complexity Adaptive Design

The optimal resource allocation for WIT corresponds to the Water-Filling (WF) strategy that assigns the amplitude of modulated tone n by

$$s_{I,n} = \sqrt{\left(\mu - \frac{\sigma_n}{P\|\mathbf{h}_n\|^2}\right)^+} \quad (35)$$

where μ is chosen to satisfy the power constraint $\|\mathbf{s}_I\|^2/2 \leq P$. The closed-form solution can be obtained by iterative power allocation and the details are omitted here. On the other hand, the Scaled Matched Filter (SMF) was proposed in [41] as a suboptimal resource allocation scheme for WPT. It involves no modulated waveform and assigns the amplitude of sinewave n by

$$s_{P,n} = \sqrt{\frac{2P}{\sum_{n=1}^N \|\mathbf{h}_n\|^{2\beta}}} \|\mathbf{h}_n\|^\beta \quad (36)$$

where the only design variable $\beta \geq 1$ scales the matched filter to exploit the rectifier nonlinearity. $\beta = 1$ corresponds to a standard matched filter where the amplitude of sinewave n is linearly proportional to the equivalent channel strength $\|\mathbf{h}_n\|$, while $\beta > 1$ further elevates the strong subchannels and suppresses the weak ones. The advantage of SMF has been experimentally demonstrated in a practical WPT system with channel acquisition [42].

To facilitate practical SWIPT implementation, we provide two low-complexity adaptive design by combining WF and SMF under TS and PS setups. The low-complexity TS scheme divides each time slot into dedicated data session with proportion $1 - \alpha$ and dedicated energy session with proportion α , then performs WF and SMF respectively. Varying α from 0 to 1 corresponds to a R-E line from WIT point to WPT point. In contrast, the low-complexity PS scheme involves the design of splitting ratio ρ as well as a superposed waveform, where the proportion of WF and SMF are controlled by a balancing ratio δ as

$$s_{I,n} = \sqrt{(1 - \delta) \left(\mu - \frac{\sigma_n}{P\|\mathbf{h}_n\|^2}\right)^+} \quad (37)$$

$$s_{P,n} = \sqrt{\frac{2\delta P}{\sum_{n=1}^N \|\mathbf{h}_n\|^{2\beta}}} \|\mathbf{h}_n\|^\beta \quad (38)$$

That is to say, the suboptimal TS scheme only need to design β while the suboptimal PS scheme should also consider ρ and δ for different R-E tradeoff.

IV. PERFORMANCE EVALUATIONS

To evaluate the performance of the proposed IRS-aided SWIPT system, we characterize the average R-E regions

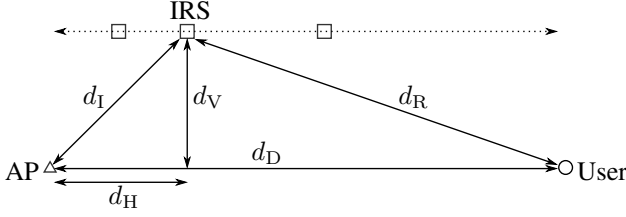


Fig. 4. System layout in the simulation.

under typical setups. Consider a large open space Wi-Fi-like environment at a center frequency of 5.18 GHz with bandwidth $B = 1$ MHz as reference. As shown in Fig. 4, we assume the IRS moves along a horizontal path parallel to the AP-user path and let d_H , d_V be the horizontal and vertical distances from the AP to the IRS, respectively. We also denote d_D , d_I , d_R as the length of direct, incident, reflective paths such that $d_I = \sqrt{d_H^2 + d_V^2}$, $d_R = \sqrt{(d_D - d_H)^2 + d_V^2}$. $d_D = 15$ m, $d_V = 2$ m and $d_H = 2$ m are chosen as reference. The path loss and fading parameters are obtained from IEEE TGN channel model D [43], and the path loss is set to $L_0 = -35$ dB at $d_0 = 1$ m. We assume all channels are NLoS with taps modelled as i.i.d. CSCG random variables of unit average sum-power, corresponding to a normalized multipath response. The reference numbers of transmit antennas, IRS elements and subbands are $M = 1$, $L = 20$, $N = 16$, respectively. No spatial correlation is assumed across transmit antennas and IRS elements. Rectenna parameters are taken as $k_2 = 0.0034$, $k_4 = 0.3829$, $R_A = 50 \Omega$ such that $\beta_2 = 0.17$ and $\beta_4 = 957.25$. The average Effective Isotropic Radiated Power (EIRP) is fixed to $P = 36$ dBm and the average noise power is $\sigma_n = -40$ dBm at all subbands as reference. We also assume a 2 dBi IRS element gain³ and a 2 dBi receive antenna gain. For the algorithm, the tolerance is set to $\epsilon = 10^{-8}$, the number of candidates in the Gaussian randomization method is set to $Q = 10^3$, and the R-E region is averaged over 300 channel realizations. In the R-E boundary, the leftmost point corresponds to WPT ($\rho = 1$) where power can be allocated simultaneously to modulated and unmodulated waveform to maximize the average output DC current. On the other hand, the rightmost point corresponds to WIT ($\rho = 0$) where the solution coincides with the Water-Filling (WF) algorithm that allocates all power to the modulated waveform only. For a fair comparison, the x -axis of the plots has been normalized to the average subband rate R/N .

We first evaluate the performance of Algorithm 1 under SDR. It is demonstrated that Φ^* is rank-1 for all tested channel realizations with different M , N and L , such that ϕ^* can be directly obtained through EVD and the Gaussian randomization step is not required. Therefore, we claim Algorithm 1 converges to stationary points of problem (24) without performance loss.

Fig. 5 illustrates the average R-E region versus the number of subband N . *First*, it is observed that increasing N reduces the average per-subband rate R/N but boosts the harvested energy. The reason is that the power budget is divided into smaller portions for each subband, but the number of balanced

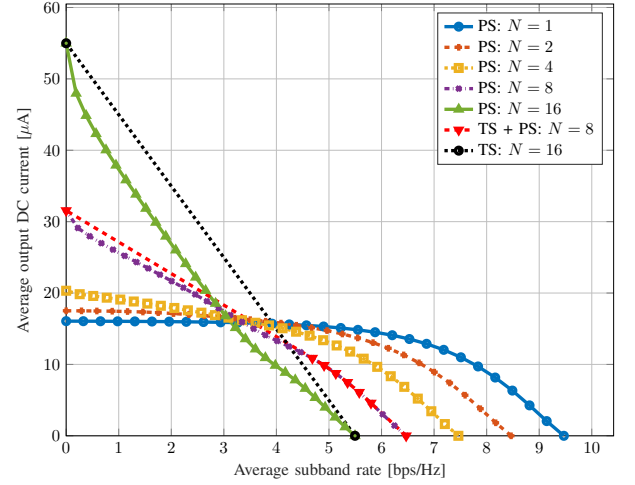


Fig. 5. Average R-E region versus N for $M = 1$, $L = 20$, $\sigma_n = -40$ dBm, $B = 1$ MHz and $d_H = d_V = 2$ m.

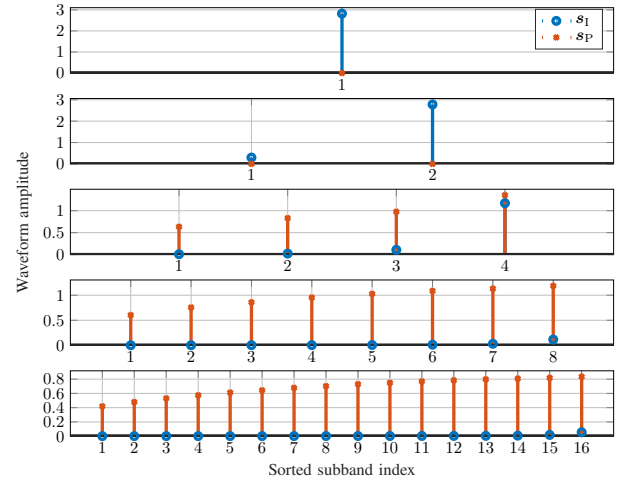


Fig. 6. WPT-optimized waveform amplitudes versus N for $M = 1$, $L = 20$, $\sigma_n = -40$ dBm, $B = 1$ MHz and $d_H = d_V = 2$ m.

DC terms m_P is increased to boost the output DC current, as suggested by the scaling laws in [12]. Sorted waveform amplitudes in Fig. 6 also confirmed that, from the perspective of WPT, a dedicated multisine waveform is unnecessary for a small N but is required for a large N . As shown in (11) and (13), the only difference between modulated and unmodulated waveform on z exists in the fourth-order terms, where $\mathbb{E}\{\mathbb{A}\{y_I^4(t)\}\}$ has N^2 monomials with a modulation gain of 2 and $\mathbb{A}\{y_P^4(t)\}$ has $(2N^3 + N)/3$ monomials without modulation gains. Therefore, the superposed waveform enlarges the R-E region for a sufficiently large N (typically no smaller than 4). *Second*, the R-E region is convex for $N = 2, 4$ and concave-convex for $N = 8, 16$. This has the consequence that PS outperforms TS for a small N and is outperformed for a large N . When N is in between, the optimal strategy is a combination of both, i.e. a time sharing between the WPT point and the saddle SWIPT point obtained by PS (as the red curve in Fig. 5). Compared with the linear harvester model that requires no dedicated power waveform and always prefer PS,

³Due to highly directional reflection.

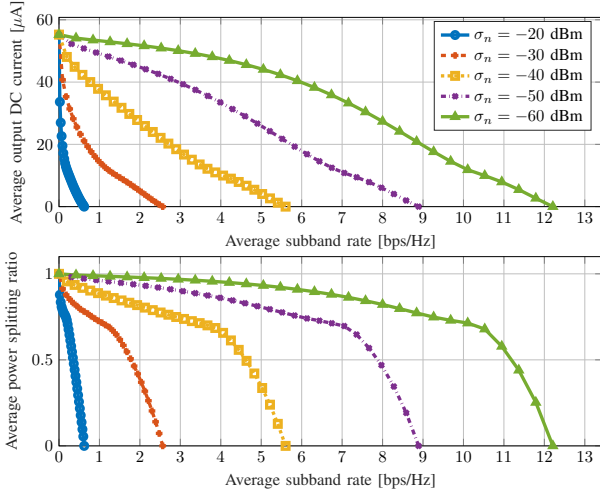


Fig. 7. Average R-E region and splitting ratio versus σ_n for $M = 1$, $N = 16$, $L = 20$, $B = 1$ MHz and $d_H = d_V = 2$ m.

the rectifier nonlinearity enlarges the R-E region by favoring a different waveform and transceiving mode, both heavily depends on N .

The influence of the average noise power on the average R-E region is investigated in Fig. 7. *First*, we note that for a large number of subbands, the R-E region is approximately concave for a high noise level while approximately convex for a low noise level. Hence, it can be concluded that TS is preferred at low SNR while PS is preferred at high SNR. This is because in the former case, the capacity-achieving WF algorithm tends to allocate more power to few strongest subbands. As the rate constraint \bar{R} decreases, more subbands are activated to further boost the harvested DC power thanks to the balancing effect among different frequencies, which originates from the harvester nonlinearity. *Second*, there exists a turning point in the R-E region especially for a small noise ($\sigma_n \leq -40$ dBm). The reason is that when \bar{R} departs slightly from the maximum achievable rate, the algorithm tends to adjust the splitting ratio ρ rather than allocating more power to the multisine waveform, as a small-amplitude multisine could be inefficient for energy maximization. On the other hand, as \bar{R} further reduces, a modulated waveform with a very large ρ could be outperformed by a superposed waveform with a smaller ρ , due to the advantage of multisine for efficient power transfer. The result highlights the benefit of dedicated power waveform and the necessity of joint optimization of waveform and splitting ratio.

In Fig. 8, we compare the average R-E region achieved by different AP-IRS horizontal distance d_H . A *first* observation is that, different from the active Amplify-and-Forward (AF) relay with the optimal development location around the midpoint [44], placing the IRS closer to either the transmitter or the receiver would further improve the R-E tradeoff. It originates from the product-distance path loss model that applies to finite-size element reflection. As shown in Fig. 9, although the piecewise TGN path loss model further penalizes large distance (greater than 10 m for model D), it is still beneficial to have a short-long or long-short transmission setup, since signal attenuation

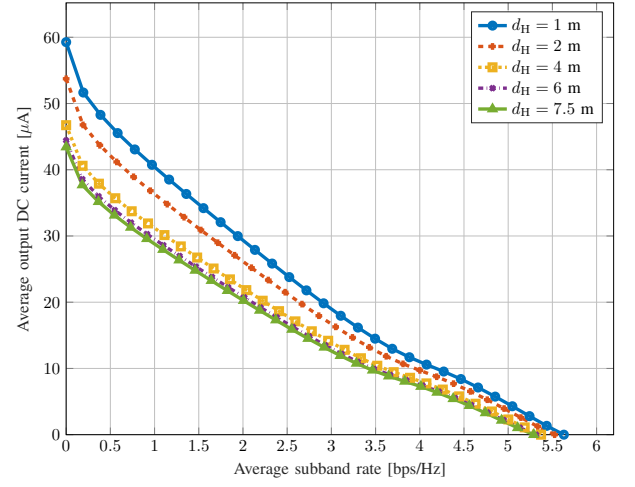


Fig. 8. Average R-E region versus d_H for $M = 1$, $N = 16$, $L = 20$, $\sigma_n = -40$ dBm, $B = 1$ MHz and $d_V = 2$ m.

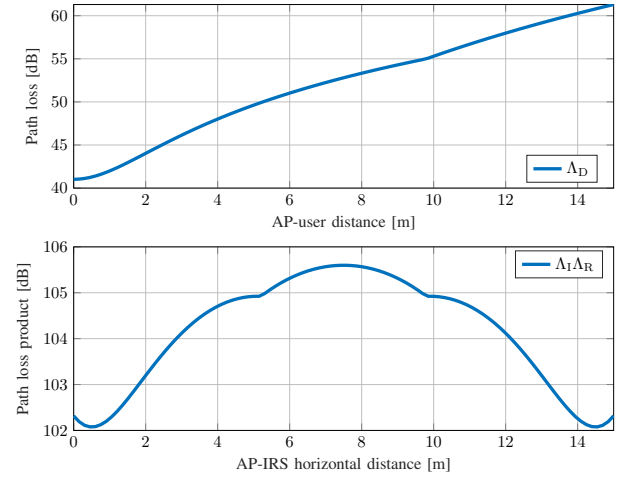


Fig. 9. Path loss versus distance for IEEE TGN channel model D.

increases fast at a short distance and experiences marginal effect at a long distance. On the other hand, it also suggests that developing an IRS next to the AP can effectively extend the operation range of SWIPT systems. Considering the passive characteristic of the IRS, opportunities are that it can be directly supported by the SWIPT network. A *second* observation from Fig. 9 is that there exist two optimal IRS development locations that minimize the path loss production $\Lambda_I \Lambda_R$. It implies that two IRSs may be implemented to further enlarge the R-E region, one attached to the AP and one attached to the user.

The number of transmit antennas M and IRS elements L influence the average R-E tradeoff as revealed in Fig. 10 and 11. *First*, it is observed that adding either active or passive elements benefits both information and power transmission. This is because increasing M or L indeed enhances the equivalent composite channel strength. *Second*, the number of active and passive elements have negligible impacts on the optimal transceiving mode (TS/PS). Unlike the noise, the channel strength influences both information and power transfer, thus varying M or L simultaneously scales both rate and current and preserves the general trend of the R-E boundary. *Third*, the

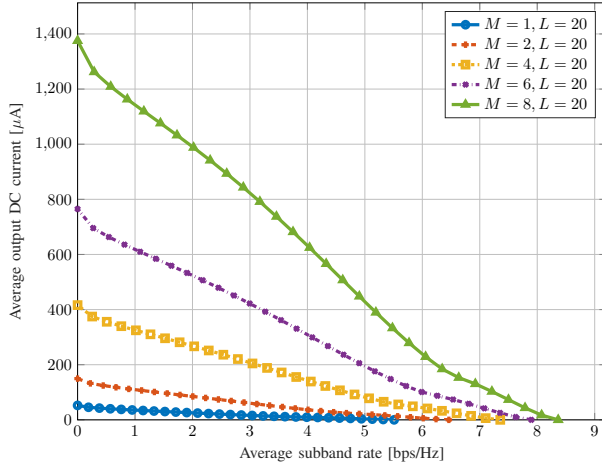


Fig. 10. Average R-E region versus M for $N = 16$, $L = 20$, $\sigma_n = -40$ dBm, $B = 1$ MHz and $d_H = d_V = 2$ m.

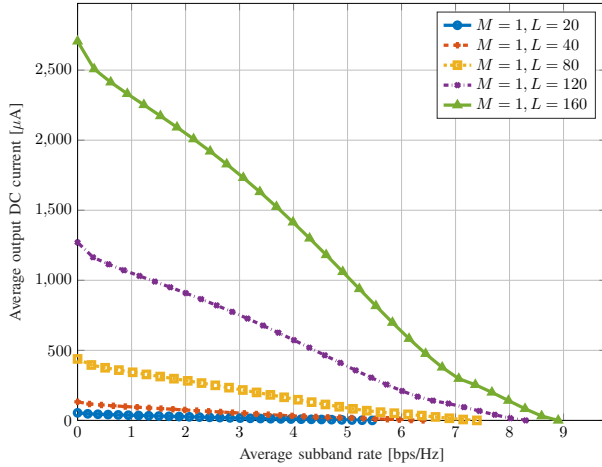


Fig. 11. Average R-E region versus L for $M = 1$, $N = 16$, $\sigma_n = -40$ dBm, $B = 1$ MHz and $d_H = d_V = 2$ m.

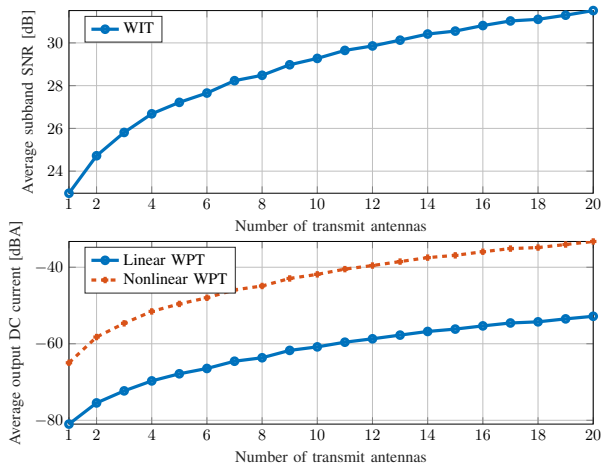


Fig. 12. Average WIT SNR and WPT DC current versus M for $L = 20$, $N = 16$, $\sigma_n = -40$ dBm, $B = 1$ MHz, $d_H = 0$ and $d_V = 0.5$ m.

passive beamforming has a larger array gain and power scaling order than the active beamforming. This behavior is more obvious in Fig. 12 and 13 that illustrate the performance of WIT

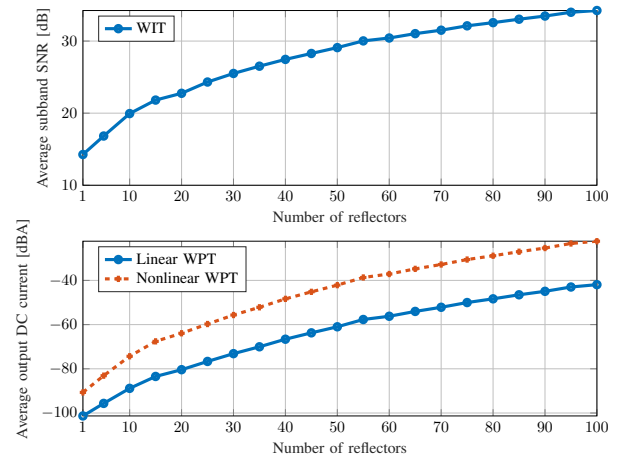


Fig. 13. Average WIT SNR and WPT DC current versus L for $M = 1$, $N = 16$, $\sigma_n = -40$ dBm, $B = 1$ MHz, $d_H = 0$ and $d_V = 0.5$ m.

and WPT only. For the active MRT beamforming, doubling M brings a 3 dB gain at the average output SNR, corresponding to a transmit array gain of M and a doubled harvester input power. Due to the rectifier nonlinearity, the output DC current ends up with a nearly four-time (12 dB) increase, validating the active scaling law in the order of M^2 [8]. On the other hand, when the IRS is very close to the transmitter or the receiver, doubling L can bring an SNR boost up to 6 dB, corresponding to a reflect array gain of L^2 . An interpretation is that the IRS coherently combines multiple signal copies with a receive array gain L , then performs an equal gain reflection with a transmit array gain L , achieving a total gain of L^2 . As a consequence, doubling IRS elements brings a four-fold boost on the received signal power that further amplifies the harvested DC current by 16 times (24 dB), suggesting a passive scaling law in the order of L^4 . Besides, by considering harvester nonlinearity, the proposed design brings a nearly 20 dB increase in the output DC current over the conventional linear perspective. These results emphasize the effectiveness of passive beamforming and the importance of modeling rectifier nonlinearity in the SWIPT system design. *Fourth*, small-scale SWIPT is dominated by the active beamforming while large-scale SWIPT relies more on the passive beamforming. As shown in Fig. 9, in our setup, the direct path loss Λ_D is around 60 dB while the auxiliary path loss product $\Lambda_I \Lambda_R$ is over 100 dB. Hence, to fully exploit the R-E advantage of passive beamforming, a large number of reflecting elements are required to enhance the auxiliary channel strength. Another explanation is that the RF-chains of active antennas provide design flexibility in the frequency domain, while the frequency-flat characteristic of the IRS restricts its benefit for broadband transmission, especially when L is small.

Fig. 14 and 15 explore the average R-E region under different IRS configuration for narrowband transmission ($B = 1$ MHz) and broadband transmission ($B = 10$ MHz). The rate-dependent adaptive IRS strategy adjusts the passive beamforming for each point on the R-E boundary, while the WIT/WPT-based non-adaptive IRS schemes only optimize the phase shifts for information and power purposes (correspond to the points

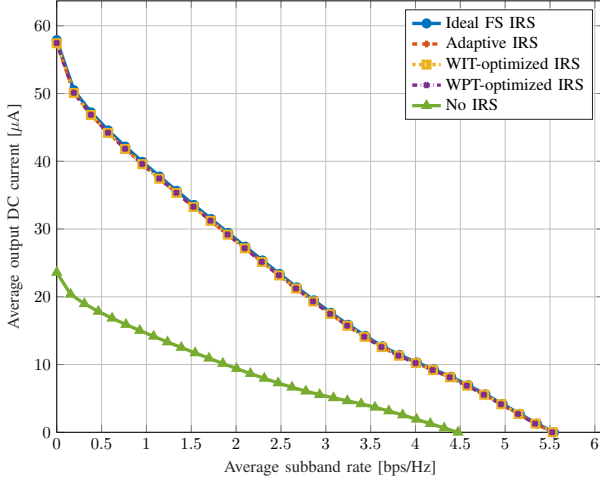


Fig. 14. Average R-E region for ideal, adaptive, fixed and no IRS over $B = 1$ MHz for $M = 1$, $N = 16$, $L = 20$, $\sigma_n = -40$ dBm and $d_H = d_V = 2$ m.

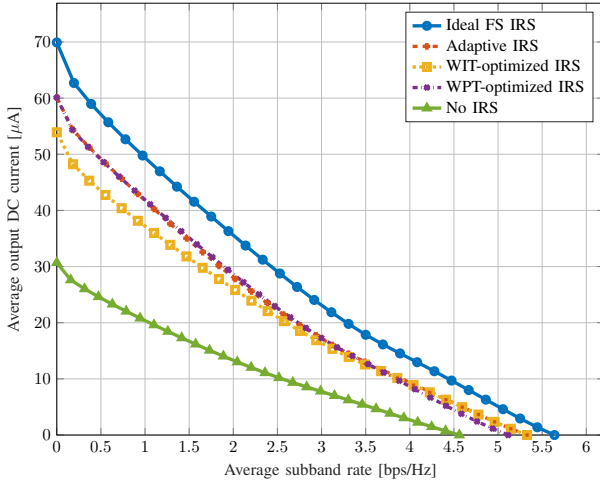


Fig. 15. Average R-E region for ideal, adaptive, fixed and no IRS over $B = 10$ MHz for $M = 1$, $N = 16$, $L = 20$, $\sigma_n = -40$ dBm and $d_H = d_V = 2$ m.

on the x and y axes, respectively). To gain some insight into the IRS behavior, we compare the results above to no IRS and an ideal Frequency-Selective (FS) IRS. In contrast to Remark 1, each element in the ideal FS IRS is assumed to have an independent reflection coefficient for each subband, accounting for NL variables in total. When there is only one transmit antenna, each ideal IRS element simply aligns the AP-IRS-user channel to the AP-user channel at all subbands, namely

$$\theta_{l,n}^* = e^{j \arg(h_{D,n}/h_{l,n,l}h_{R,n,l})}, \quad \forall n, l. \quad (39)$$

First, it is observed that the assistance of the IRS effectively enlarges the achievable R-E region for both narrowband and broadband transmissions. Second, the performance of all four IRS strategies coincide with each other for narrowband SWIPT. It suggests that the optimal passive beamforming obtained for any R-E point is also optimal for the whole R-E region. Therefore, for a given channel, we can fix the active and passive

beamforming, and only adapt the waveform and splitting ratio to achieve different R-E performance. This is because when the bandwidth is small, all channels are approximately flat such that the optimal ideal reflection coefficients at all subbands are approximately the same. Also, the subchannel tradeoff in Remark 1 does not exist as the auxiliary channel can be simultaneously maximized at different frequencies. Third, a joint optimization of waveform, active and passive beamforming, and splitting ratio is necessary to maximize the R-E tradeoff for broadband SWIPT. Recall Remark 2 that WIT and WPT prefer different subchannel strength distribution. By adaptive passive beamforming, the channel strength can either be concentrated in few strongest subbands to enhance the rate at a low SNR, or be spread evenly over all subbands to boost the output DC power. The advantage of such a smart channel control is prominent for broadband SWIPT where the strength can vary significantly for different subbands.

V. CONCLUSION AND FUTURE WORKS

This paper proposes a novel IRS-aided multi-carrier downlink MISO SWIPT system to enhance the rate and energy tradeoff of a single user. We perform a joint optimization of the waveform and active beamforming at the transmitter, the passive beamforming at the IRS, and the power splitting ratio at the receiver to enlarge the achievable R-E region. Different from the existing IRS-aided SWIPT literature, this paper leverages rectifier nonlinearity in passive beamforming design and investigates a multi-carrier transmission for practical co-localized receiver architectures. Efficient algorithms based on the AO, SCA, SDR and GP techniques are numerically demonstrated feasible for all tested channel realizations under different configurations. We confirm that considering harvester nonlinearity, a dedicated power waveform is generally required to boost the R-E tradeoff. When developed near the transmitter, the IRS can provide effective channel enhancement to enlarge the R-E region and expand the operation range. Compared with the transmit antenna, the IRS element has no design flexibility in the frequency domain, but it integrates the coherent combining and transmission techniques in a fully passive manner to further boost the array gain and power scaling effects. Finally, the optimal passive beamforming at any R-E point is also optimal for the whole R-E region of narrowband transmission, and the rate-dependent adaptive passive beamforming is beneficial for broadband transmission.

The combination of IRS and SWIPT brings many possibilities and challenges. For example, how to optimize the waveform, active and passive beamforming in a multi-user SWIPT system? How can multiple IRS cooperate with each other to further benefit the R-E tradeoff? How to perform channel estimation without RF-chains at the IRS? How to design an IRS-aided SWIPT system for different multiple access techniques? How to develop SWIPT in new networks, such as cell-free massive Multiple-Input Multiple-Output (MIMO)? Can IRS operation be directly supported by SWIPT? Answers to these questions may bring a new wireless revolution.

REFERENCES

- [1] B. Clerckx, R. Zhang, R. Schober, D. W. K. Ng, D. I. Kim, and H. V. Poor, "Fundamentals of wireless information and power transfer: From RF energy harvester models to signal and system designs," *IEEE Journal on Selected Areas in Communications*, vol. 37, no. 1, pp. 4–33, 2019.
- [2] L. R. Varshney, "Transporting information and energy simultaneously," *IEEE International Symposium on Information Theory - Proceedings*, pp. 1612–1616, 2008.
- [3] X. Zhou, R. Zhang, and C. K. Ho, "Wireless information and power transfer: Architecture design and rate-energy tradeoff," *IEEE Transactions on Communications*, vol. 61, no. 11, pp. 4754–4767, 2013.
- [4] R. Zhang and C. K. Ho, "MIMO broadcasting for simultaneous wireless information and power transfer," *IEEE Transactions on Wireless Communications*, vol. 12, no. 5, pp. 1989–2001, 2013.
- [5] J. Park and B. Clerckx, "Joint wireless information and energy transfer in a K-user MIMO interference channel," *IEEE Transactions on Wireless Communications*, vol. 13, no. 10, pp. 5781–5796, 2014.
- [6] M. S. Trotter, J. D. Griffin, and G. D. Durgin, "Power-optimized waveforms for improving the range and reliability of RFID systems," *2009 IEEE International Conference on RFID, RFID 2009*, pp. 80–87, 2009.
- [7] B. Clerckx and J. Kim, "On the Beneficial Roles of Fading and Transmit Diversity in Wireless Power Transfer with Nonlinear Energy Harvesting," *IEEE Transactions on Wireless Communications*, vol. 17, no. 11, pp. 7731–7743, 2018.
- [8] B. Clerckx and E. Bayguzina, "Waveform Design for Wireless Power Transfer," *IEEE Transactions on Signal Processing*, vol. 64, no. 23, pp. 6313–6328, 2016.
- [9] J. Kim, B. Clerckx, and P. D. Mitcheson, "Experimental Analysis of Harvested Energy and Throughput Trade-off in a Realistic SWIPT System," in *2019 IEEE Wireless Power Transfer Conference (WPTC)*. IEEE, jun 2019, pp. 1–5.
- [10] —, "Signal and System Design for Wireless Power Transfer : Prototype, Experiment and Validation," *IEEE Transactions on Wireless Communications*, vol. 1276, no. c, pp. 1–1, 2020.
- [11] J. Kim and B. Clerckx, "Range Expansion for Wireless Power Transfer: A Joint Beamforming and Waveform Architecture," *arXiv preprint arXiv:2010.01680*.
- [12] B. Clerckx, "Wireless Information and Power Transfer: Nonlinearity, Waveform Design, and Rate-Energy Tradeoff," *IEEE Transactions on Signal Processing*, vol. 66, no. 4, pp. 847–862, 2018.
- [13] M. Varasteh, B. Rassouli, and B. Clerckx, "On Capacity-Achieving Distributions for Complex AWGN Channels Under Nonlinear Power Constraints and Their Applications to SWIPT," *IEEE Transactions on Information Theory*, vol. 66, no. 10, pp. 6488–6508, 2020.
- [14] —, "SWIPT Signaling over Frequency-Selective Channels with a Nonlinear Energy Harvester: Non-Zero Mean and Asymmetric Inputs," *IEEE Transactions on Communications*, vol. 67, no. 10, pp. 7195–7210, 2019.
- [15] M. Varasteh, J. Hoydis, and B. Clerckx, "Learning to Communicate and Energize: Modulation, Coding and Multiple Access Designs for Wireless Information-Power Transmission," *IEEE Transactions on Communications*, vol. 6778, no. DL, pp. 1–1, 2020.
- [16] D. H. Kim and J. I. Choi, "Design of a multiband frequency selective surface," *ETRI Journal*, vol. 28, no. 4, pp. 506–508, 2006.
- [17] R. S. Anwar, L. Mao, and H. Ning, "Frequency selective surfaces: A review," *Applied Sciences (Switzerland)*, vol. 8, no. 9, pp. 1–47, 2018.
- [18] T. J. Cui, M. Q. Qi, X. Wan, J. Zhao, and Q. Cheng, "Coding metamaterials, digital metamaterials and programmable metamaterials," *Light: Science & Applications*, vol. 3, no. 10, pp. e218–e218, 2014.
- [19] C. Liaskos, S. Nie, A. Tsoliariidou, A. Pitsillides, S. Ioannidis, and I. Akyildiz, "Realizing Wireless Communication Through Software-Defined HyperSurface Environments," *19th IEEE International Symposium on a World of Wireless, Mobile and Multimedia Networks, WoWMoM 2018*, 2018.
- [20] Q. Wu and R. Zhang, "Intelligent Reflecting Surface Enhanced Wireless Network: Joint Active and Passive Beamforming Design," in *2018 IEEE Global Communications Conference (GLOBECOM)*, vol. 18, no. 11. IEEE, dec 2018, pp. 1–6.
- [21] —, "Beamforming Optimization for Intelligent Reflecting Surface with Discrete Phase Shifts," in *ICASSP 2019 - 2019 IEEE International Conference on Acoustics, Speech and Signal Processing (ICASSP)*. IEEE, may 2019, pp. 7830–7833.
- [22] —, "Intelligent Reflecting Surface Enhanced Wireless Network via Joint Active and Passive Beamforming," *IEEE Transactions on Wireless Communications*, vol. 18, no. 11, pp. 5394–5409, nov 2019.
- [23] S. Abeywickrama, R. Zhang, and C. Yuen, "Intelligent Reflecting Surface: Practical Phase Shift Model and Beamforming Optimization," in *ICC 2020 - 2020 IEEE International Conference on Communications (ICC)*. IEEE, jun 2020, pp. 1–6. [Online]. Available: <https://ieeexplore.ieee.org/document/9148961/>
- [24] Q.-U.-A. Nadeem, A. Kammoun, A. Chaaban, M. Debbah, and M.-S. Alouini, "Intelligent Reflecting Surface Assisted Wireless Communication: Modeling and Channel Estimation," *arXiv preprint arXiv:1906.02360*, pp. 1–7, 2019.
- [25] Y. Yang, S. Zhang, and R. Zhang, "IRS-Enhanced OFDMA: Joint Resource Allocation and Passive Beamforming Optimization," *IEEE Wireless Communications Letters*, pp. 1–1, 2020.
- [26] L. Dai, M. D. Renzo, C. B. Chae, L. Hanzo, B. Wang, X. Yang, J. Tan, S. Bi, S. Xu, F. Yang, and Z. Chen, "Reconfigurable Intelligent Surface-Based Wireless Communications: Antenna Design, Prototyping, and Experimental Results," *IEEE Access*, vol. 8, pp. 45 913–45 923, 2020.
- [27] Q. Wu and R. Zhang, "Weighted Sum Power Maximization for Intelligent Reflecting Surface Aided SWIPT," *IEEE Wireless Communications Letters*, vol. 9, no. 5, pp. 586–590, 2020.
- [28] Y. Tang, G. Ma, H. Xie, J. Xu, and X. Han, "Joint Transmit and Reflective Beamforming Design for IRS-Assisted Multiuser MISO SWIPT Systems," in *ICC 2020 - 2020 IEEE International Conference on Communications (ICC)*. IEEE, jun 2020, pp. 1–6.
- [29] Q. Wu and R. Zhang, "Joint Active and Passive Beamforming Optimization for Intelligent Reflecting Surface Assisted SWIPT Under QoS Constraints," *IEEE Journal on Selected Areas in Communications*, vol. 38, no. 8, pp. 1735–1748, aug 2020.
- [30] C. Pan, H. Ren, K. Wang, M. ElKashlan, A. Nallanathan, J. Wang, and L. Hanzo, "Intelligent Reflecting Surface Aided MIMO Broadcasting for Simultaneous Wireless Information and Power Transfer," *IEEE Journal on Selected Areas in Communications*, pp. 1–33, 2020.
- [31] M. Piñuela, P. D. Mitcheson, and S. Lucyszyn, "Ambient RF energy harvesting in urban and semi-urban environments," *IEEE Transactions on Microwave Theory and Techniques*, vol. 61, no. 7, pp. 2715–2726, 2013.
- [32] Y. Huang and B. Clerckx, "Large-Scale Multiantenna Multisine Wireless Power Transfer," *IEEE Transactions on Signal Processing*, vol. 65, no. 21, pp. 5812–5827, 2017.
- [33] T. Adali and S. Haykin, *Adaptive Signal Processing*. Hoboken, NJ, USA: John Wiley & Sons, Inc., mar 2010.
- [34] Y. Huang and D. P. Palomar, "Rank-constrained separable semidefinite programming with applications to optimal beamforming," *IEEE Transactions on Signal Processing*, vol. 58, no. 2, pp. 664–678, 2010.
- [35] M. C. Grant and S. P. Boyd, "CVX: Matlab software for disciplined convex programming, version 2.0 beta," 2013. [Online]. Available: <http://cvxr.com/cvx/>
- [36] S. Boyd, S. J. Kim, L. Vandenbergh, and A. Hassibi, "A tutorial on geometric programming," *Optimization and Engineering*, vol. 8, no. 1, pp. 67–127, 2007.
- [37] M. Chiang, *Geometric programming for communication systems*, 2005, vol. 2, no. 1.
- [38] B. R. Marks and G. P. Wright, "A General Inner Approximation Algorithm for Nonconvex Mathematical Programs," *Operations Research*, vol. 26, no. 4, pp. 681–683, 1978.
- [39] W. C. Li, T. H. Chang, C. Lin, and C. Y. Chi, "Coordinated beamforming for multiuser MISO interference channel under rate outage constraints," *IEEE Transactions on Signal Processing*, vol. 61, no. 5, pp. 1087–1103, 2013.
- [40] L. Grippo and M. Sciandrone, "On the convergence of the block nonlinear Gauss-Seidel method under convex constraints," *Operations Research Letters*, vol. 26, no. 3, pp. 127–136, 2000.
- [41] B. Clerckx and E. Bayguzina, "Low-Complexity Adaptive Multisine Waveform Design for Wireless Power Transfer," *IEEE Antennas and Wireless Propagation Letters*, vol. 16, no. 1, pp. 2207–2210, 2017.
- [42] J. Kim, B. Clerckx, and P. D. Mitcheson, "Prototyping and experimentation of a closed-loop wireless power transmission with channel acquisition and waveform optimization," *WPTC 2017 - Wireless Power Transfer Conference*, pp. 1–4, 2017.
- [43] V. Erceg, "TGN Channel Models," in *IEEE 802.11-03/940r4*, 2004.
- [44] S. Li, K. Yang, M. Zhou, J. Wu, L. Song, Y. Li, and H. Li, "Full-Duplex Amplify-and-Forward Relaying: Power and Location Optimization," *IEEE Transactions on Vehicular Technology*, vol. 66, no. 9, pp. 8458–8468, 2017.